DOI: 10.1002/anie.201307689

Electron Microscopy

Fluorine in Shark Teeth: Its Direct Atomic-Resolution Imaging and Strengthening Function**

Chunlin Chen, Zhongchang Wang, Mitsuhiro Saito, Tetsuya Tohei, Yoshiro Takano, and Yuichi Ikuhara*

Abstract: *Atomic-resolution imaging of beam-sensitive biominerals is extremely challenging, owing to their fairly complex structures and the damage caused by electron irradiation. Herein, we overcome these difficulties by performing aberration-corrected electron microscopy with low-dose imaging techniques, and report the successful direct atomic-resolution imaging of every individual atomic column in the complex fluorapatite structure of shark tooth enameloid, which can be of paramount importance for teeth in general. We demonstrate that every individual atomic column in shark tooth enameloid can be spatially resolved, and has a complex fluorapatite structure. Furthermore, ab initio calculations show that fluorine atoms can be covalently bound to the surrounding calcium atoms, which improves understanding of their caries-reducing effects in shark teeth.*

Biominerals, which are created by living organisms,[1] and their formation are of considerable significance in many areas of biological science, ranging from vital physiological processes such as bone growth and tooth development to pathological processes such as formation of kidney and salivary stones.[2–4] Structures of biominerals reveal key information for understanding these processes, and offer a basis for inferring biomineralization mechanisms,[5–8] as well as establishing novel material concepts, such as organic–inorganic composites.[9,10] For decades, transmission electron microscopy (TEM) has been used to characterize biominerals,[11–15] but it offers, at best, structural information at the nanoscale, due to the damage caused by the electron beam. In particular, owing to their incorporation with organics, biominerals are much more sensitive to such damage than their inorganic counterparts. Efforts to gain atomic-level knowledge of biominerals are further complicated by their fairly complex structures. Recent advances in aberration-corrected TEM and scanning TEM (STEM) allow direct imaging with single-atom sensitivity,[16–20] but such resolution is again hampered by a combination of extremely weak signals, arising from light atoms in biominerals, and damage induced by the electron beam. Herein, we overcome these difficulties by performing aberration-corrected electron microscopy with a low-dose imaging technique,[21–24] and report the successful direct atomic-resolution imaging of shark tooth enameloid, which can be of paramount importance for teeth in general. We demonstrate that every individual atomic column in the complex fluorapatite structure of shark tooth enameloid can be spatially resolved, and find that fluorine atoms can be covalently bound to calcium, which has implications for the understanding of their caries-reducing effects in teeth.[25–27] To the best of our knowledge, this demonstrates, for the first time, a combined study of atomic-resolution imaging and first-principles calculations on biominerals, which facilitates the investigation of biominerals from the nanoscale to the atomic scale.

Elucidating the mechanism of biologically governed biomineralization, a process by which living organisms produce the minerals that offer a basis for multifunctional activity or structural support, requires a priori knowledge of the fine structure of biominerals, especially at the atomic level. Several experimental methods can be used to characterize biominerals, but with the majority of them it is difficult to provide enough information to obtain an atomic solution to their structures. X-ray spectroscopy and backscattering yield an ensemble average of a whole sample, and hence fall short of providing atomic resolution. Scanning tunneling microscopy can offer insights into atomic-scale features, but is restricted by sample conductivity. TEM should, in principle, be able to achieve atomic resolution.[17,18] However, the atomic-scale structure of biominerals remains challenging to resolve, as a normal voltage does damage to beam-sensitive biominerals, whereas a low one downgrades resolution. Herein, we use low-dose imaging techniques to minimize electron beam damage, and demonstrate the direct imaging of

[*] Dr. C. L. Chen, Prof. Z. C. Wang, Dr. M. Saito, Prof. Y. Ikuhara
WPI Research Center, Advanced Institute for Materials Research
Tohoku University
2-1-1 Katahira, Aoba-ku, Sendai 980-8577 (Japan)
E-mail: zcwang@wpi-aimr.tohoku.ac.jp
Dr. T. Tohei, Prof. Y. Ikuhara
Institute of Engineering Innovation, The University of Tokyo (Japan)
Prof. Y. Takano
Section of Biostructural Science, Graduate School of Tokyo Medical and Dental University (Japan)
Prof. Y. Ikuhara
Nanostructures Research Laboratory (Japan) Fine Ceramics Center (Japan)

[**] This work was conducted in part in the Research Hub for Advanced Nano Characterization at the University of Tokyo, and supported by "Nanotechnology Platform", both sponsored by the MEXT of Japan. C.C. acknowledges support from a Grant-in-Aid for Young Scientists (B) (24760532). Z.C.W. is thankful for financial support from a Grant-in-Aid for Young Scientists (A) (24686069), Challenging Exploratory Research (24656376), a Sasakawa Scientific Research Grant, and the JGC-S Foundation. M.S. is grateful to the Grant-in-Aid for Scientific Research (C) (23560817) and the IKETANI and IZUMI Foundation for financial support. Y.T. is thankful for a Grant-in-Aid for Scientific Research (B) (24390408). Calculations were conducted at the ISSP, University of Tokyo.

Supporting information for this article is available on the WWW under http://dx.doi.org/10.1002/anie.201307689.

every individual atom in shark tooth enameloid, especially fluorine. Such a direct atomic-resolution imaging of fluorine has been pursued by dental scientists for decades, yet remained elusive, despite its importance to the the dental field because it forms the basis for deep understanding of caries-reducing effects.

Shark teeth probably represent the healthiest teeth of all living creatures owing to their enameloid, the hard and compact outmost portion that envelops the softer dentin. Despite its pivotal importance, our knowledge of enameloid microstructures remains at the micrometer scale; for example, it consists of a high density of fluorapatite crystals and a low content of organic matrix (5–8 wt.%).[28] The fluorapatite crystals are distributed over the surfaces of shark teeth (Figure 1a), as revealed in energy-dispersive X-ray spectroscopy (EDS) mapping (Supporting Information, Figure S1). Moreover, it consists of well-arranged fibrous crystal bundles with a diameter of a few micrometers. Although it is known that the bundles grow along a specific topological direction,[28] the atomic-scale structure of the interiors of the fibrous fluorapatite bundles remains missing, thus limiting our fundamental understanding on tooth enameloid.

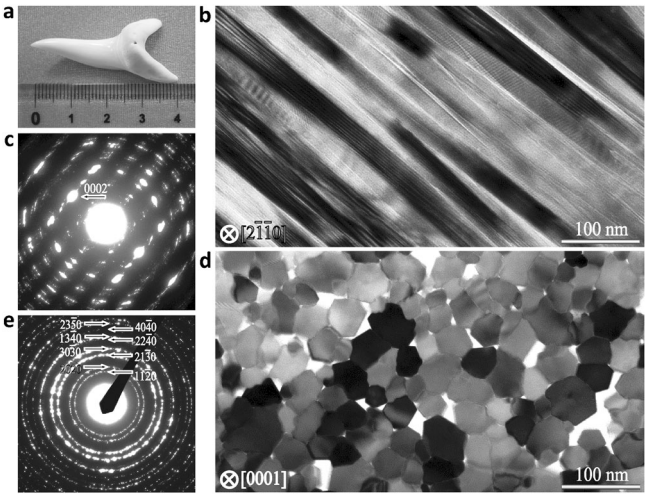

Figure 1. Shark tooth microstructure. a) Photograph of a shark tooth. b) Bright-field TEM image and c) corresponding SAED pattern taken along the [2$\bar{1}\bar{1}$0] direction (perpendicular to the longitudinal axis of the fluorapatite bundles). d) TEM image and e) SAED patterns taken along [0001] (cross-section of the fluorapatite bundles).

Figure 1 shows bright-field TEM images and selected-area electron diffraction (SAED) patterns for the tooth enameloid of a shark of the species oxyrinchus. The enameloid consists of bunches of single-crystalline nanorods with a diameter of ca. 50 nm (Figure 1b). The SAED pattern identifies the longitudinal axis of the nanorods as [0001], because of the (0002) diffraction spots (arrow in Figure 1c). This morphology is confirmed in the TEM image taken along the longitudinal axis of the nanorods (Figure 1d), revealing a textured feature. Under most circumstances, the nanorods are in atomic contact, with no secondary-phase layers, contaminants, or transition areas in between, as confirmed by high-resolution TEM (HRTEM; Figure S2). On inspection of the SAED pattern of a cross-section, we identify all diffraction rings as belonging to the [0001] zone axis (Figure 1d), thus offering definitive evidence that the nanorods grow along [0001]. Further systematic characterization of an individual nanorod testifies this growth mode in shark tooth enameloid (Figure S3).

To extract atomic-resolution structural information, we obtained orthogonal HRTEM images taken along [2$\bar{1}\bar{1}$0] and [0001] (Figure S4). Although a periodic image contrast is observed, it remains difficult to resolve each individual atomic column owing to the spherical aberration of the magnetic lens and the complex fluorapatite structure ($Ca_5(PO_4)_3F$). To gain atomic detail, we performed aberration-corrected TEM with a low-dose electron beam to directly resolve all atoms in the fluorapatite from [0001]. The [0001] zone axis was purposely chosen because all elements in the fluorapatite can form atomic columns along this direction (Figure 2a), thereby increasing the likelihood of visualizing all of them at atomic resolution.

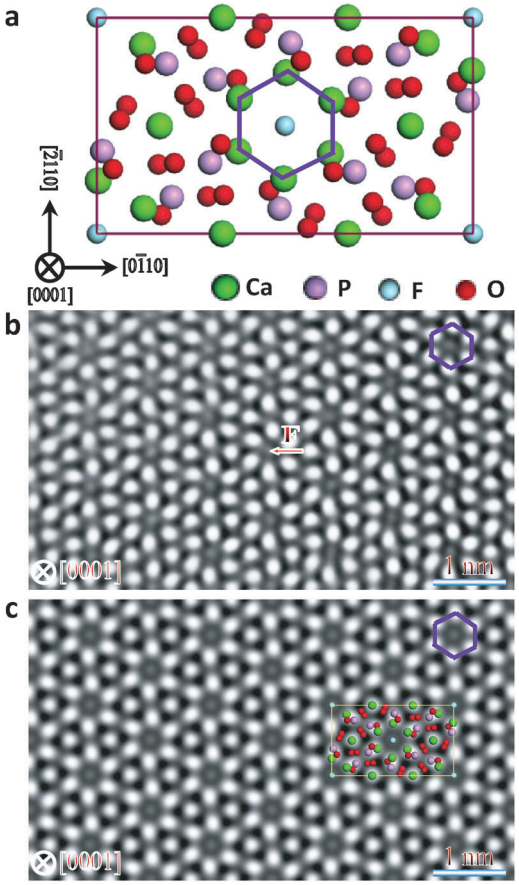

Figure 2. Atomic-resolution HRTEM image of a shark tooth. a) Atomic model of fluorapatite viewed from the [0001] direction. b) Aberration-corrected HRTEM image taken along the [0001] zone axis. The image shows periodically aligned hexagonal units (marked) with a clear bright spot at their center. c) Simulated HRTEM image along the [0001] direction. An atomic model of fluorapatite is overlapped on the image. Bright spots in a hexagon represent the very closely spaced Ca, P, and O atomic columns. The bright spot at the center of each hexagon represents an F atom.

The low-dose method is realized by taking a smaller condenser aperture and dispersing the electron beam in a wide area. Figure 2b shows an HRTEM image taken along [0001]. Surprisingly, every individual atomic column can be unambiguously identified, notwithstanding the low dose technique. Periodically arranged hexagonal units (marked in Figure 2b) with a single bright spot at their center can be observed. This structure agrees with the relaxed model of fluorapatite, and the bright spots around the hexagons were identified as being comprised of Ca, P, O, and F atoms (Figure 2a). We further conducted a series of image simulations as a function of the focus and sample thickness (Figure S5), and found that the specimen is 2.8 nm thick and each bright spot represents an atomic column. In comparing simulated HRTEM images (Figure 2c) with experimental ones (Figure 2b), we found good agreement, leading to the conclusion that the bright spots at the six apexes of each hexagon represent Ca, P, and O atoms, with F atoms as the central spots.

To identify each individual atomic column and shed light on their atomic density, we further perform Cs-corrected STEM. To solve the damage issue arising from the focused electron beam, we relied on the low-dose imaging techniques, and acquire atomic-resolution high-angle annular-dark-field (HAADF) and annular-bright-field (ABF) images.[29,30] The probe current is assumed to be ca. 3 pA (dose rate: ca. $3.7\times10^{27}\,e\,s^{-1}\,m^{-2}$), which almost represents the lowest available for STEM. Figure 3a presents a raw HAADF STEM image, which can only be obtained by a fast scan before the specimen suffers damage. This image is one of the best (to our knowledge) atom-resolved images ever attained for a beam-sensitive biomineral. As the intensity of an atomic column in HAADF mode is proportional to $Z^{1.7}$ (Z = atomic number),[31] contrast in the image is brighter for heavier atoms. In addition, contrast also relies on atomic density. Clearly, there emerge two types of Ca in the fluorapatite: one has a much stronger contrast (labeled Ca1) and the other a relatively weaker one (labeled Ca2), which is attributed to the double atomic density of Ca1 columns compared to Ca2 columns. Unfortunately, the much lighter F and O atoms are not scattered strongly enough to be visualized in the HAADF image, rendering it incomplete.

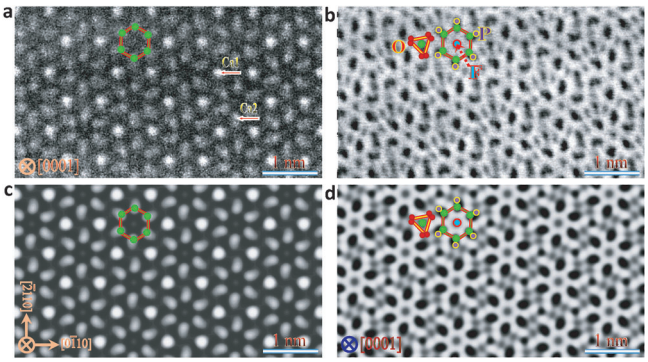

Figure 3. Identifying each individual atomic column in a shark tooth. a) HAADF and b) ABF STEM images viewed along [0001]. Ca1 columns have a much brighter image contrast than Ca2 owing to the double atomic density of Ca1 compared to Ca2. The F and O atomic columns cannot be identified in the HAADF, but can in the ABF STEM image. The F atoms sit at the center of the hexagons formed by Ca2 atoms. P atoms are situated close to the Ca2 atoms. In the ABF image, there are three slightly expanded dark spots surrounding Ca1, forming an equilateral triangle. Each spot represents two very closely spaced O atomic columns. c,d) Simulated HAADF (c) and ABF STEM (d) images viewed from the [0001] direction. The simulated images match the experimental ones.

To directly resolve all atomic columns, an ABF STEM image (Figure 3b)[30] was collected simultaneously with the HAADF image. In addition to conveying the identical structural information as the HAADF, the ABF STEM image, in which dark spots represent atomic columns, can indeed reveal all atomic columns in the fluorapatite. The F atoms sit at center of the hexagons formed by the Ca2 atoms. Near to the hexagons, three elongated dark spots (indicated in Figure 3b) form an equilateral triangle, and each of them can be recognized as two very closely spaced O atoms. The Ca1 atoms were found to sit at the center of the triangles. As a final confirmation, we simulated HAADF (Figure 3c) and ABF STEM (Figure 3d) images and compared them with their experimental counterparts (Figure 3a,b). A good agreement was obtained, demonstrating that atom-by-atom structural and chemical resolving of all atoms in the beam-sensitive biominerals is now becoming possible.

The discovery that fluoride has an excellent caries-reducing effect is a landmark in the history of dentistry.[25–27] Direct atomic-resolution imaging of all atomic columns in teeth, particularly the F atoms, is a critical step forward in our understanding of teeth strengthening. Although it is known that the cariostatic impact of fluoride on teeth implicates a complex biological and environmental process,[25,32] the fluorine should be of paramount importance in stabilizing fluorapatite, because its loss would directly lead to *c*-empty defective metastable apatite $Ca_5(PO_4)_3$.[33] To gain insight into the effects of fluorine from the viewpoint of materials science and to support the imaging, we further performed density-functional-theory (DFT) calculations. The optimum lattice constants of fluorapatite were calculated to be 100.8% of the experimental values,[33] and the calculated band gap (5.7 eV) is close to that previously reported (5.9 eV).[33]

To identify the bonding type directly, contour and isosurface plots of charge density and density difference along the (0001) plane were examined (Figure 4). The (0001) plane slices through the central F and Ca hexagons, and the P–O pairs, thus allowing us to extract maximum bonding information. Interestingly, the charge distribution on F is almost spherically symmetric, with lobes toward neighboring Ca, which indicates that the bonding in the hexagons is of mixed covalent–ionic nature. The covalency is verified in the isosurface plot (Figure 4b), revealing a charge connection between F and Ca atoms from the strong hybridization of Ca pd orbitals with F p orbitals. This is interesting in view of the strong electronegativity of F and the fact that the Ca–F bonding in CaF_2 is ionic.[34,35] Furthermore, because covalent bonds are generally believed to be stronger than ionic ones,[36,37] the presence of covalency in the Ca–F bonds suggests that F is critical to stabilizing the hexagonal frames, namely, the loss of

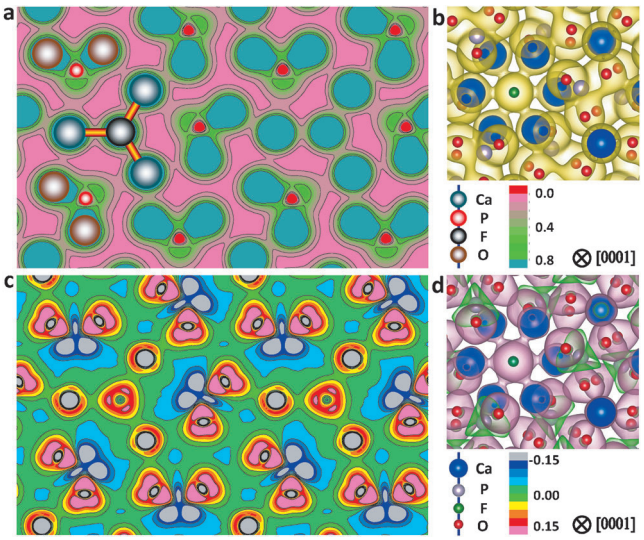

Figure 4. Identifying bonding type in fluorapatite. a) Planar contour plot of charge density viewed along the (0001) plane slicing through F ions at the center of the hexagons. b) Isosurface of charge density viewed along the [0001] direction, highlighting the region surrounding a hexagon. c) Planar plot of charge density difference seen along the same plane as in the density map. Charge density difference represents charge redistribution in the fluorapatite relative to its isolated system. d) Isosurface of charge-density difference viewed along the same plane as in the density map. Isosurface in blue denotes negative values (loss of electrons), whereas that in pink denotes positive ones (gain of electrons).

F to form the *c*-empty $Ca_5(PO_4)_3$ weakens teeth. From the density difference plot, we noticed a charge accumulation along the Ca–F bond lines. The charges on F atoms come predominantly from the adjacent Ca atom (Figure 4c,d). The P–O bonds show a greater degree of covalency, as charges on the O ions are more severely distorted towards neighboring P atoms owing to the stronger hybridization between the p orbitals of the O and P atoms. Evidently, the charge distribution is more pronounced between P and O atoms than between Ca and F atoms, implying that the P–O bond is stronger than Ca–F. This suggests that the Ca–F bond is the strength-limiting bond in teeth, thus highlighting the importance of directly imaging F atoms. Moreover, O atoms gain charges at the expense of charge loss on the neighboring P atoms (Figure 4c,d). These DFT calculations are the first attempt to clarify the strengthening function of fluorine in teeth from the aspects of atomic and electronic structures, although such an explanation is not the only one.

In conclusion, despite years of effort to solve the structural issues, resolving the exact site of all atoms in beam-sensitive biominerals with single-atom sensitivity remains a considerable challenge, particularly for those with a fairly complex geometry. Our results offer definitive evidence that this has now become possible through aberration-corrected electron microscopy in combination with low-dose techniques. Such direct imaging of fluorine and the identification of covalent bonds offers a basis for fundamental understanding of the teeth-strengthening function of fluorine. Although demonstrated with shark teeth, the present techniques could, in principle, be used to image other classes of biominerals at atomic resolution, which holds substantial promise for decoding associated biomineralization processes in general.

Experimental Section

Microscopic characterization: The thin-foil specimen for (S)TEM observations was prepared by cutting, grinding, dimpling, and Ar-ion-beam thinning. EDS mapping was conducted using an electron-probe X-ray microanalyzer (SHIMADZU EPMA-8705) at 15 kV. The size of electron beam was 65 μm and the beam current was 20 nA. SAED patterns, TEM, and HRTEM images were taken using a JEM-2010F (JEOL Co. Ltd.) with an accelerating voltage of 200 kV. Aberration-corrected HRTEM images were taken at 300 kV using a FEI TITAN80–300 electron microscope equipped with an image corrector. The spherical value was −38.9 μm and over focus was ca. 20 nm. The dose rate of electron beam was evaluated as ca. 2×10^{22} $e\,s^{-1}\,m^{-2}$, which is 2–10% of the value adopted in standard HRTEM techniques. The HAADF and ABF images were taken with a 200 kV STEM (JEM-ARM200F, JEOL) equipped with a probe corrector (CEOS, Gmbh). A probe current of ca. 3 pA (dose rate: ca. 3.7×10^{27} $e\,s^{-1}\,m^{-2}$) was used. Image simulations were conducted by the WinHREM package (see the Supporting Information).

Calculation methods: DFT calculations were conducted using the VASP.[39] The projector-augmented wave (PAW) method was employed for electron-ion interaction and the generalized gradient approximation (PW91) was applied to address exchange-correlation functional. We used a cutoff energy of 400 eV and *k* points of $3\times3\times4$. The fluorapatite was modeled by a periodic supercell with size of $16.41\times18.95\times6.96$ Å. All atoms were fully relaxed until the magnitude of force on every atom fell to <0.05 e Å^{-1}.

Received: September 1, 2013
Revised: October 27, 2013
Published online: January 20, 2014

Keywords: ab initio calculations · biominerals · ceramics · electron microscopy

[1] P. U. P. A. Gilbert, M. Abrecht, B. H. Frazer, *Rev. Mineral. Geochem.* **2005**, *59*, 157–185.
[2] J. Aizenberg, J. C. Weaver, M. S. Thanawala, V. C. Sundar, D. E. Morse, P. Fratzl, *Science* **2005**, *309*, 275–278.
[3] G. He, T. Dahl, A. Veis, A. George, *Nat. Mater.* **2003**, *2*, 552–558.
[4] J. D. Rimer, Z. An, Z. Zhu, M. H. Lee, D. S. Goldfarb, J. A. Wesson, M. D. Ward, *Science* **2010**, *330*, 337–341.
[5] C. S. Chan, G. D. Stasio, S. A. Welch, M. Girasole, B. H. Frazer, M. V. Nesterova, S. Fakra, J. F. Banfield, *Science* **2004**, *303*, 1656–1658.
[6] L. Addadi, S. Weiner, *Nature* **1997**, *389*, 912–915.
[7] C. Sollner, M. Burghammer, E. Busch-Nentwich, J. Berger, H. Schwarz, C. Riekel, T. Nicolson, *Science* **2003**, *302*, 282–286.
[8] Y. Politi, T. Arad, E. Klein, S. Weiner, L. Addadi, *Science* **2004**, *306*, 1161–1164.
[9] S. Kamat, X. Su, R. Ballarini, A. H. Heuer, *Nature* **2000**, *405*, 1036–1040.
[10] J. Aizenberg, D. A. Muller, J. L. Grazul, D. R. Hamann, *Science* **2003**, *299*, 1025–1028.
[11] D. Fortin, *Science* **2004**, *303*, 1618–1619.
[12] V. Imbeni, J. J. Kruzic, G. W. Marshall, S. J. Marshall, R. O. Ritchie, *Nat. Mater.* **2005**, *4*, 229–232.
[13] S. Boonrungsiman, E. Gentleman, R. Carzaniga, N. D. Evans, D. W. McComb, A. Porter, M. M. Stevens, *Proc. Natl. Acad. Sci. USA* **2012**, *109*, 14170–14175.

[14] F. Nudelman, K. Pieterse, A. George, P. H. H. Bomans, H. Friedrich, L. J. Brylka, P. A. J. Hilbers, G. D. With, N. A. J. M. Sommerdijk, *Nat. Mater.* **2010**, *9*, 1004 – 1008.
[15] L. M. Gordon, D. Joester, *Nature* **2011**, *469*, 194 – 198.
[16] C. L. Jia, M. Lentzen, K. Urban, *Science* **2003**, *299*, 870 – 873.
[17] P. D. Nellist, M. F. Chisholm, N. Dellby, O. L. Krivanek, M. F. Murfitt, Z. S. Szilagyi, A. R. Lupini, A. Borisevich, W. H. Sides, Jr., S. J. Pennycook, *Science* **2004**, *305*, 1741.
[18] N. Shibata, S. D. Findlay, S. Azuma, T, Mizoguchi, T. Yamamoto, Y. Ikuhara, *Nat. Mater.* **2009**, *8*, 654 – 658.
[19] R. Ishikawa, N. Shibata, F. Oba, T. Taniguchi, S. D. Findlay, I. Tanaka, Y. Ikuhara, *Phys. Rev. Lett.* **2013**, *110*, 065504.
[20] O. L. Krivanek, M. F. Chisholm, V. Nicolosi, T. J. Pennycook, G. J. Corbin, N. Dellby, M. F. Murfitt, C. S. Own, Z. S. Szilagyi, M. P. Oxley, S. T. Pantelides, S. J. Pennycook, *Nature* **2010**, *464*, 571 – 574.
[21] V. Ortalan, A. Uzun, B. C. Gates, N. D. Browning, *Nat. Nanotechnol.* **2010**, *5*, 506 – 510.
[22] M. Malac, M. Beleggia, R. Egerton, Y. M. Zhu, *Ultramicroscopy* **2007**, *107*, 40 – 49.
[23] J. P. Buban, Q. Ramasse, B. Gipson, N. D. Browning, H. Stahlberg, *J. Electron Microsc.* **2010**, *59*, 103 – 112.
[24] "Low-Dose Imaging Techniques for Transmission Electron Microscopy": D. B. Carlson, J. E. Evans in *The Transmission Electron Microscope* (Ed.: K. Maaz), InTech, Rijeka, Croatia, **2012**, pp. 85 – 98, ISBN: 978-953-51-0450-6.
[25] T. Aoba, *Crit. Rev. Oral Biol. Med.* **1997**, *8*, 136 – 153.
[26] H. C. Margolis, E. C. Moreno, B. J. Murphy, *J. Dent. Res.* **1986**, *65*, 23 – 29.
[27] L. Wong, T. W. Cutress, J. F. Duncan, *J. Dent. Res.* **1987**, *66*, 1735 – 1741.
[28] J. Enax, O. Prymak, D. Raabe, M. Apple, *J. Struct. Biol.* **2012**, *178*, 290 – 299.
[29] S. D. Findlay, N. Shibata, H. Sawada, E. Okunishi, Y. Kondo, Y. Ikuhara, *Ultramicroscopy* **2010**, *110*, 903 – 923.
[30] S. D. Findlay, N. Shibata, H. Sawada, E. Okunishi, Y. Kondo, T. Yamamoto, Y. Ikuhara, *Appl. Phys. Lett.* **2009**, *95*, 191913 – 1 – 3.
[31] S. J. Pennycook, L. A. Boatner, *Nature* **1988**, *336*, 565 – 567.
[32] K. Matsunaga, *J. Am. Ceram. Soc.* **2010**, *93*, 1 – 14.
[33] L. Calderín, M. J. Stott, A. Rubio, *Phys. Rev. B* **2003**, *67*, 134106.
[34] R. Saravanana, S. Israel, *Physica B* **2004**, *352*, 220 – 226.
[35] S. Ossicini, C. Arcangeli, O. Bisi, *Phys. Rev. B* **1991**, *43*, 9823 – 9830.
[36] *Understanding of bioinstruments* (Ed.: M. Prakash), Discovery Publishing House PVT. LTD., New Delhi, India, **2009**, p. 195.
[37] *The Wiley Encyclopedis of Packing Technology* (Ed.: K. L. Yam), Wiley, Hoboken, **2009**, p. 1167.
[38] E. J. Kirkland, *Advanced computing in electron microscopy*, Springer, New York, **1998**.
[39] G. Kresse, J. Furthmüller, *Phys. Rev. B* **1996**, *54*, 11169 – 11186.

